



Three-dimensionally ordered macroporous $\text{Eu}_{0.6}\text{Sr}_{0.4}\text{FeO}_3$ supported cobalt oxides: Highly active nanocatalysts for the combustion of toluene

Kemeng Ji, Hongxing Dai*, Jiguang Deng, Liyun Song, Baozu Gao, Yuan Wang, Xinwei Li

Laboratory of Catalysis Chemistry and Nanoscience, Department of Chemistry and Chemical Engineering, College of Environmental and Energy Engineering, Beijing University of Technology, Beijing 100124, PR China

ARTICLE INFO

Article history:

Received 20 June 2012

Received in revised form 1 September 2012

Accepted 6 October 2012

Available online 13 October 2012

Keywords:

Three-dimensionally ordered macroporous

perovskite-type oxide

Toluene combustion

Templating preparation method

Supported cobalt oxide catalyst

ABSTRACT

Three-dimensionally ordered macroporous (3DOM) $\text{Eu}_{0.6}\text{Sr}_{0.4}\text{FeO}_3$ -supported cobalt oxide nanocatalysts ($\text{yCoO}_x/\text{3DOM-ESFO}$; $\text{y wt\%} = 1, 3, 6, \text{ and } 10$) were prepared using the incipient wetness impregnation method. Physicochemical properties of the composite materials were characterized by means of numerous techniques, and their catalytic performance was evaluated for the combustion of toluene. It is shown that all of the samples displayed a well-defined 3DOM architecture with a surface area of $22\text{--}31\text{ m}^2\text{ g}^{-1}$ and the loaded cobalt oxide nanoparticles with a diameter of $7\text{--}11\text{ nm}$ were well dispersed on the surface of the 3DOM-ESFO support. Among the $\text{yCoO}_x/\text{3DOM-ESFO}$ samples, the $3\text{CoO}_x/\text{3DOM-ESFO}$ and $6\text{CoO}_x/\text{3DOM-ESFO}$ ones possessed the highest oxygen adspecies concentration and the best reducibility at low temperature, and hence showing the best catalytic performance (the temperatures required for 50 and 90% toluene conversions were ca. 250 and 270°C at a space velocity of $20,000\text{ mL g}^{-1}\text{ h}^{-1}$, respectively) for toluene combustion. The apparent activation energies (ca. 72 kJ mol^{-1}) of $3\text{CoO}_x/\text{3DOM-ESFO}$ and $6\text{CoO}_x/\text{3DOM-ESFO}$ were lower than that (81 kJ mol^{-1}) of 3DOM-ESFO. It is concluded that the enhanced catalytic performance of $3\text{CoO}_x/\text{3DOM-ESFO}$ and $6\text{CoO}_x/\text{3DOM-ESFO}$ for toluene combustion was mainly related to their higher oxygen adspecies concentrations, stronger reducibility at low temperature, and better dispersion of cobalt oxide nanoparticles.

© 2012 Elsevier B.V. All rights reserved.

1. Introduction

Most of volatile organic compounds (VOCs) emitted from industrial and transportation activities are environmental pollutants. Catalytic combustion can be regarded as one of the most effective and economical alternatives for the abatement of VOCs [1,2], in which the commonly used catalysts reported in the literature are noble metals and transition metal oxides [2–4]. In spite of high performance at low temperatures, the applications of noble metal (e.g., Pt, Pd, and Rh [5])-based catalysts are limited due to their high cost, low thermal stability, easy sintering, and tendency to poisoning [3,6,7]. As a potential alternative of noble metals, perovskite-type oxides (ABO_3) have received considerable attention in the catalytic oxidation of VOCs [8] due to their low price, anti-poisoning capability, and high thermal stability. The catalytic performance of such mixed oxides is generally associated with factors, such as oxygen nonstoichiometry, reducibility, surface area, and pore structure [9]. They can be tailor-made by the partial substitution of the A- and/or B-site cations in ABO_3 with foreign cations (e.g., $\text{La}_{1-x}\text{Sr}_x\text{FeO}_3$ [10] and $\text{La}_{1-x}\text{Sr}_x\text{CoO}_3$ [11])

to obtain enhanced catalytic performance [7]. Many researchers reported that $\text{La}_{1-x}\text{Sr}_x\text{MO}_3$ ($\text{M} = \text{Co}$ or Mn) showed better catalytic activity when the x was equal to 0.4 [2,6,12,13]. In recent years, the hard-templating strategy is one of effective pathways to obtain three-dimensionally ordered macroporous (3DOM) ABO_3 with large surface areas and developed pore structures, such as 3DOM-structured LaFeO_3 (surface area = $21\text{--}32\text{ m}^2\text{ g}^{-1}$) [14], $\text{La}_{1-x}\text{Sr}_x\text{FeO}_3$ (surface area = $24\text{--}49\text{ m}^2\text{ g}^{-1}$) [15], Au/LaFeO_3 (surface area = $31\text{--}32\text{ m}^2\text{ g}^{-1}$) [16], $\text{LaCo}_x\text{Fe}_{1-x}\text{O}_3$ [17], and $\text{La}_{1-x}\text{K}_x\text{CoO}_3$ [18]. It has been demonstrated that some simple transition metal oxides (MO_x , e.g., MnO_x [19] and CoO_x [20]) are active for the oxidation of VOCs, though they are less in thermal stability and inferior in catalytic activity to precious metals [21,22]. However, the MO_x often plays a positive role in enhancing catalytic performance of an ABO_3 . For instance, the presence of excess MnO_x in LaMnO_3 could improve the stability and catalytic activity of the perovskite for the removal of automotive exhaust pollutants [23]; ZrO_2 was also reported to increase the catalytic activities of LaNiO_3 for NO_x reduction with CO [24] and of LaCoO_3 and LaFeO_3 for CO oxidation [24]. There have been other reports on the preparation of perovskite-loaded transition metal oxide catalysts, for example, $\text{Co}_3\text{O}_4/\text{LaCoO}_3$ [25], $\text{Co}_3\text{O}_4/\text{Ba}_{0.5}\text{Sr}_{0.5}\text{Co}_{0.8}\text{Fe}_{0.2}\text{O}_{3-\delta}$ [12], $\text{Co}_3\text{O}_4/\text{LaFe}_{0.7}\text{Cu}_{0.3}\text{O}_3$ [26], and $\text{Fe}_2\text{O}_3/\text{La}_{0.6}\text{Sr}_{0.4}\text{Co}_{0.8}\text{Fe}_{0.2}\text{O}_{3-\delta}$ [27,28]. The ABO_3 supports used in the above studies, however, are all nonporous. Since porous ABO_3

* Corresponding author. Tel.: +86 10 6739 6118; fax: +86 10 6739 1983.

E-mail address: hxdai@bjut.edu.cn (H. Dai).

can provide good dispersion of active components on their surfaces, it would be better to prepare the $\text{MO}_x/\text{3DOM-ABO}_3$ catalysts that show large surface areas and developed pore structures.

In the past years, our group have been devoting to the fabrication and physicochemical property characterization of metal oxides (e.g., $\gamma\text{-Al}_2\text{O}_3$ (surface area = $145\text{ m}^2\text{ g}^{-1}$) [29], $\alpha\text{-Fe}_2\text{O}_3$ (surface area = $32\text{--}46\text{ m}^2\text{ g}^{-1}$) [30]) and 3DOM-structured ABO_3 (e.g., LaMnO_3 (surface area = $10\text{--}40\text{ m}^2\text{ g}^{-1}$) [31,32], $\text{SrFeO}_{3-\delta}$ (surface area = $34\text{--}61\text{ m}^2\text{ g}^{-1}$) [33]) by using the poly(methyl methacrylate) (PMMA)-templating method. However, $\text{Eu}_{1-x}\text{Sr}_x\text{FeO}_3$ ($x = 0$ and 0.4) has not been investigated in the catalytic removal of VOCs. It was reported that CeO_2 -supported Co_3O_4 nanocatalysts exhibited high activities for CO and VOC oxidation, in which an improved thermal stability and enhanced redox ability were observed [34]. Furthermore, the synergistic action was present between CoO_x and ABO_3 . Therefore, we envision that highly dispersing CoO_x onto the 3DOM-structured $\text{Eu}_{0.6}\text{Sr}_{0.4}\text{FeO}_3$ surface can generate composite catalysts that would show enhanced catalytic performance for the combustion of VOCs. Herein, we report the preparation, characterization, and catalytic activities of $\text{Eu}_{0.6}\text{Sr}_{0.4}\text{FeO}_3$ (ESFO)-supported cobalt oxide catalysts for the complete oxidation of toluene.

2. Experimental

2.1. Catalyst preparation

The 3DOM-structured ESFO support was prepared according to the citric acid-assisted PMMA-templating method. Europium, strontium, and iron nitrates at a Eu/Sr/Fe molar ratio of $0.6/0.4/1.0$ were dissolved in a mixture solution of ethylene glycol (EG), methanol (MeOH), and deionized water (with the volumetric ratio of EG/MeOH/ H_2O at $2/4/5$) as well as an equal molar ratio of citric acid to the total metal ions, giving the total metal ion concentration of ca. 1.3 mol L^{-1} . The hard-template PMMA microspheres synthesized according to the procedures described elsewhere [29] and well-arranged in three-dimensional arrangement by evaporation self-assembly were ca. 300 nm in average diameter. A certain amount of PMMA (1.0 g per 0.01 mol metal ions) was soaked in the above solution for 4 h , filtered, dried, and firstly calcined in a N_2 flow of 20 mL min^{-1} at 500°C for 3 h , and after being cooled to 50°C in the same atmosphere, the as-obtained material was further heated in an air flow of 20 mL min^{-1} to 750°C for 4 h . In order to obtain the high-quality 3DOM-structured ESFO material, a slow heating rate of 1°C min^{-1} was adopted in both calcination steps.

The $\text{yCoO}_x/\text{3DOM-ESFO}$ catalysts were prepared using the incipient wetness impregnation method. In a typical preparation, the desired amount of cobalt nitrate was first dissolved in a specific volume of deionized water. 0.2 g of the 3DOM-ESFO support was then impregnated with the cobalt nitrate solution. The mixture was dried at 70°C overnight, heated in air (60 mL min^{-1}) at a ramp of 1°C min^{-1} from RT to 400°C and maintained at this temperature for 4 h . The obtained catalysts were denoted as $\text{yCoO}_x/\text{3DOM-ESFO}$ ($y\text{ wt}\%$ was the weight percentage of Co_3O_4 , $y\text{ wt}\% = 1, 3, 6, \text{ and } 10$).

2.2. Catalyst characterization

The X-ray powder diffraction (XRD) patterns of the catalysts were obtained on a Bruker D8 Advance equipment with $\text{Cu K}\alpha$ radiation and Ni filter ($\lambda = 0.15406\text{ nm}$) at 40 kV and 35 mA . The scanning electron microscopic (SEM) images were recorded on a Gemini Zeiss Supra 55 apparatus operating at 10 kV . The transmission electron microscopic (TEM) images and selected-area electron diffraction (SAED) patterns of the samples were collected on a JEOL-2010 equipment operating at 200 kV . The specific surface areas of the catalysts were measured via N_2 adsorption at -196°C on

Micromeritics ASAP 2020 by the Brunauer–Emmett–Teller (BET) method, and the pore-size distributions were calculated according to the Barrett–Joyner–Halenda (BJH) method. Before BET measurements, the samples were degassed at 250°C for 2 h under vacuum. X-ray photoelectron spectroscopy (XPS) analyses were performed on a VG CLAM 4 MCD analyzer (with resolution at 0.5 eV) to collect the surface information of the samples. The X-ray excitation source was $\text{Mg K}\alpha$ ($h\nu = 1253.6\text{ eV}$). The spectra of the samples were recorded in the analysis chamber ($3 \times 10^{-9}\text{ Torr}$) after they were pretreated in an O_2 flow of 20 mL min^{-1} at 600°C for 1 h and then degassed in the primary chamber (10^{-5} Torr) for 0.5 h . All of the obtained binding energies (BEs) of Eu 3d, Sr 3d, Fe 2p, Co 2p, O 1s, and C 1s were calibrated against the C 1s signal (BE = 284.6 eV) of contaminant carbon.

Hydrogen temperature-programmed reduction (H_2 -TPR) experiments were conducted on a Micromeritics Auto Chem II 2920 apparatus. Before each run, the sample (30 mg , $40\text{--}60\text{ mesh}$) was first pretreated in an O_2 flow (30 mL min^{-1}) at 300°C for 1 h in a quartz fixed-bed U-shaped microreactor (i.d. = 4 mm). When it cooled to RT in the O_2 atmosphere, a $5\% \text{ H}_2/\text{Ar}$ (v/v) flow of 50 mL min^{-1} was fed to the catalyst bed and maintained for 0.5 h to purge excessive oxygen on the catalyst surface. After the baseline was stable, the sample was heated to 900°C at a ramp of $10^\circ\text{C min}^{-1}$. The outlet gases were measured on-line by the thermal conductivity detector (TCD) of the Micromeritics Auto Chem II 2920 apparatus. The TCD responses of the samples were calculated according to the calibration against the total reduction of mass-known CuO powders (Alfa Aesar, 99.9995%).

2.3. Catalytic evaluation

Catalytic activity measurements were carried out in a fixed-bed flow quartz microreactor (i.d. = 4 mm) at atmospheric pressure, with a mixture of 0.1 g of catalyst ($40\text{--}60\text{ mesh}$) and 0.3 g of quartz sands ($40\text{--}60\text{ mesh}$) packed in the middle of the tubular microreactor. The total flow rate of the reactant feed (1000 ppm toluene + $\text{O}_2 + \text{N}_2$ (balance)) was of 33.3 mL min^{-1} , with the toluene/ O_2 molar ratio and space velocity (SV) being $1/400$ and ca. $20,000\text{ mL g}^{-1}\text{ h}^{-1}$, respectively. For the change in SV, we altered the mass of the catalyst. The 1000 ppm toluene fed to the microreactor was generated by passing a N_2 flow through a toluene-filling container immersed in an ice-water isothermal bath. The products were analyzed using a gas chromatograph (GC-2010, Shimadzu) equipped with a flame ionization detector (FID) and a TCD, using a capillary column (Chromosorb 101) for organic gas separation and a packing column (Carboxen 1000) for permanent gas separation. Prior to each run, the catalyst was treated with the reactant mixture at 100°C for 1.5 h to avoid overestimation (caused by adsorption) of toluene conversion. The balance of carbon throughout the investigations was reckoned to be 99.5% . Toluene (C_7H_8) conversion ($X\%$) and specific toluene consumption rate (r ($\mu\text{mol g}^{-1}\text{ s}^{-1}$)) normalized per catalyst mass (m_{cat}) were respectively calculated as follows:

$$X\% = \frac{[(\text{C}_7\text{H}_8)_{\text{in}} - (\text{C}_7\text{H}_8)_{\text{out}}]}{(\text{C}_7\text{H}_8)_{\text{in}}} \times 100,$$

and $r = (\text{C}_7\text{H}_8)_{\text{in}} \times X\% / m_{\text{cat}} = \text{SV} \times X\% \times 1.24256 \times 10^{-7}$ ($\mu\text{mol g}^{-1}\text{ s}^{-1}$), where $(\text{C}_7\text{H}_8)_{\text{in}}$ and $(\text{C}_7\text{H}_8)_{\text{out}}$ refers to the inlet and outlet toluene concentrations.

3. Results and discussion

3.1. Crystal phase structure

Fig. 1 shows the 3DOM-ESFO and $\text{yCoO}_x/\text{3DOM-ESFO}$ ($y\text{ wt}\% = 1, 3, 6, \text{ and } 10$) samples. By comparing to the XRD pattern of

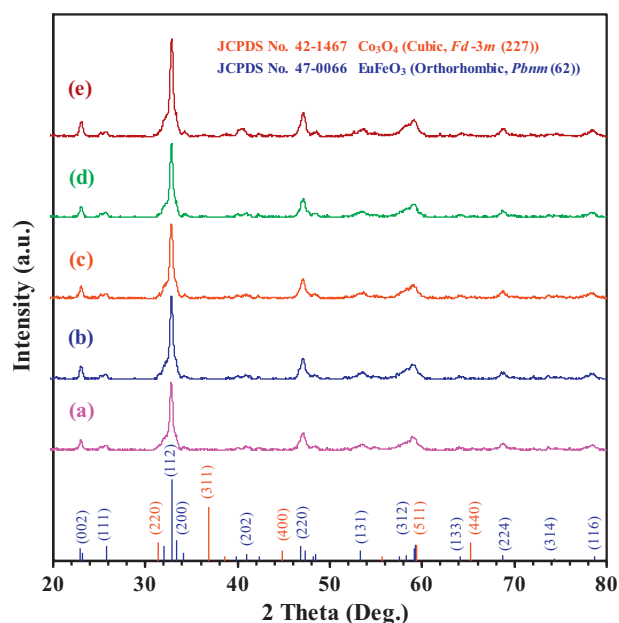


Fig. 1. XRD patterns of (a) 3DOM-ESFO, (b) 1CoO_x/3DOM-ESFO, (c) 3CoO_x/3DOM-ESFO, (d) 6CoO_x/3DOM-ESFO, and (e) 10CoO_x/3DOM-ESFO.

the standard EuFeO₃ sample (JCPDS PDF# 47-0066, *Pbnm*(62)), one can deduce that the 3DOM-ESFO sample was of single-phase orthorhombic perovskite structure. The XRD patterns of the yCoO_x/3DOM-ESFO samples were rather similar to that of the ESFO-3DOM sample, and there was no detection of diffraction signals assignable to cubic Co₃O₄ (JCPDS PDF# 42-1467, *Fd-3m*(227)) in the yCoO_x/3DOM-ESFO (y wt% = 1, 3, and 6) samples. In addition to weak XRD signals due to the cubic Co₃O₄ phase in the 10CoO_x/3DOM-ESFO sample, however, there were an extraordinary peak at $2\theta = \text{ca. } 40^\circ$, ascribable to the lattice distortion induced by the excess Co₃O₄. A discrepancy in crystallinity of the 3DOM-ESFO and yCoO_x/3DOM-ESFO samples could be reflected by the crystal sizes of these samples (Table 1). When the loading of cobalt oxide was low, the crystal sizes of yCoO_x/3DOM-ESFO (y wt% = 1, 3, and 6) were basically the same (ca. 25.8 nm) and slightly bigger than that (25.2 nm) of the ESFO-3DOM sample. When the loading of Co₃O₄ increased to 10 wt%, the crystal size of 10CoO_x/3DOM-ESFO ascended to ca. 26.3 nm. This result indicates that through the calcination at 400 °C, the cobalt oxides at a low loading were probably highly dispersed on the 3DOM-structured ESFO surface, whereas at a high loading of Co₃O₄ we could not exclude the possibility of cobalt incorporation into the lattice of 3DOM-structured Eu_{0.6}Sr_{0.4}FeO₃.

3.2. Morphology, pore structure, and surface area

Figs. 2 and 3 show the representative SEM and TEM images as well as the SAED patterns of the 3DOM-ESFO and yCoO_x/3DOM-ESFO samples, respectively. It is observed from Fig. 2 that all of the samples displayed a 3DOM structure, with the quality of 3DOM structure being different from each other. The macropore size and wall thicknesses of 3DOM-ESFO were 160–180 and 20–30 nm, respectively, and the small windows interconnecting macropores were 70–80 nm in diameter. As it can be seen from Fig. 2b, the wall of 3DOM-ESFO was smooth. With the loading of cobalt oxide, there was the presence of CoO_x nanoparticles on the surface of 3DOM-ESFO, especially in the case of 10CoO_x/3DOM-ESFO (Fig. 2h). Obviously, through the process of incipient wetness impregnation, these composite catalysts still maintained high-quality (i.e., highly aligned) 3DOM structure. As can be seen from Fig. 3, all

Table 1
Preparation parameters, average crystallite sizes, BET surface areas, and pore volumes of the 3DOM-ESFO and yCoO_x/3DOM-ESFO catalysts.

Catalyst	Co ₃ O ₄ loading (wt%)	Calcination condition	Crystal phase	<i>D</i> ^a (nm)	Surface area (m ² g ⁻¹)		Pore volume (cm ³ g ⁻¹)	
					Macropore	Mesopore	Total	Total
3DOM-ESFO	–	500 °C for 3 h in N ₂ → 750 °C for 4 h in air	Orthorhombic perovskite	25.2	10.5	20.8	31.3	0.063
1CoO _x /3DOM-ESFO	1	400 °C for 4 h in air	Orthorhombic perovskite	25.8	4.7	17.9	22.6	0.114
3CoO _x /3DOM-ESFO	3	400 °C for 4 h in air	Orthorhombic perovskite	25.8	2.5	21.6	24.1	0.108
6CoO _x /3DOM-ESFO	6	400 °C for 4 h in air	Orthorhombic perovskite	25.8	4.4	23.4	27.8	0.120
10CoO _x /3DOM-ESFO	10	400 °C for 4 h in air	Orthorhombic perovskite + cubic Co ₃ O ₄	26.3	12.4	10.0	22.4	0.057

^a Data calculated according to the full width at half-maximum of the (1 1 2) XRD line and the Scherrer equation.

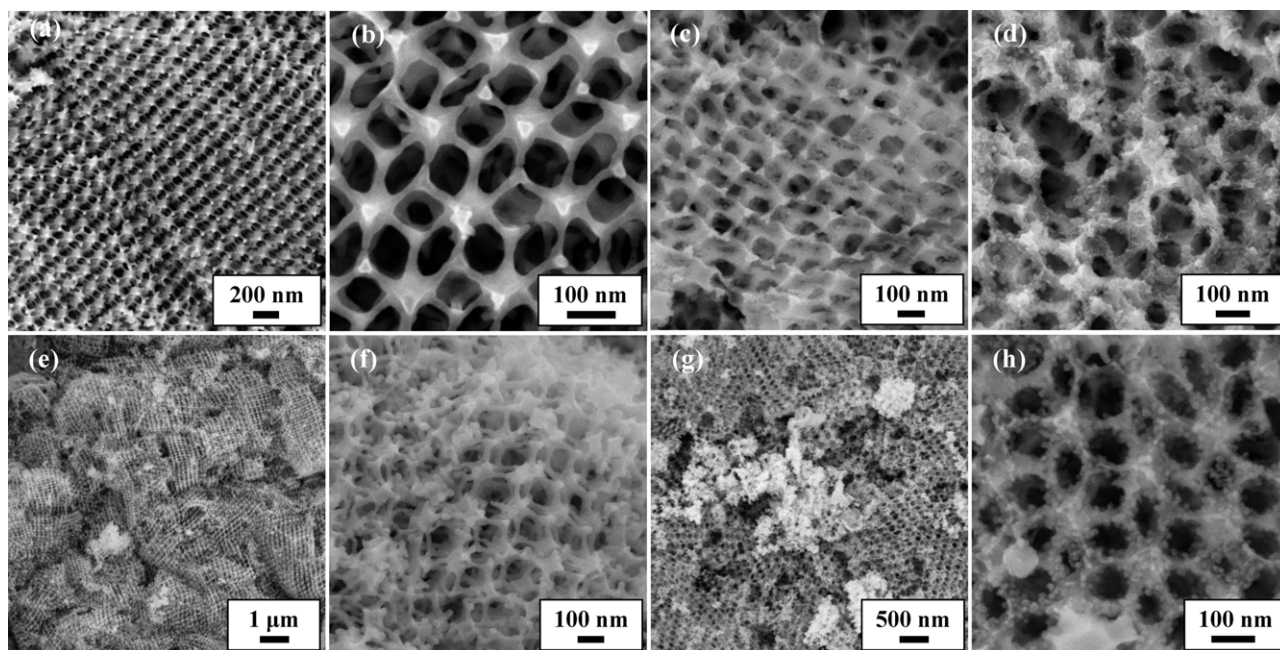


Fig. 2. SEM images of (a and b) 3DOM-ESFO, (c) 1CoO_x/3DOM-ESFO, (d) 3CoO_x/3DOM-ESFO, (e and f) 6CoO_x/3DOM-ESFO, and (g and h) 10CoO_x/3DOM-ESFO.

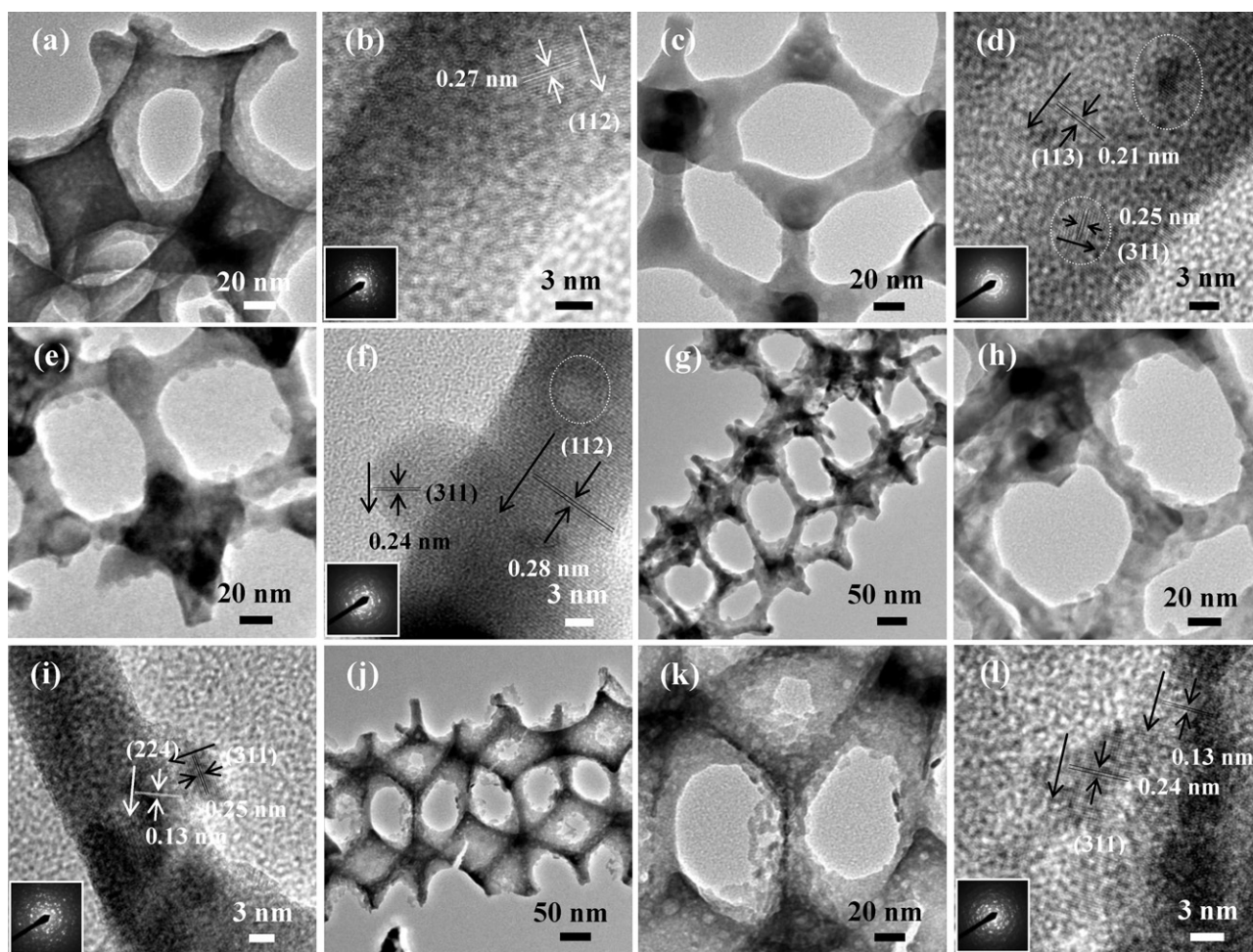


Fig. 3. TEM images and SAED patterns (insets) of (a and b) 3DOM-ESFO, (c and d) 1CoO_x/3DOM-ESFO, (e and f) 3CoO_x/3DOM-ESFO, (g–i) 6CoO_x/3DOM-ESFO, and (j–l) 10CoO_x/3DOM-ESFO.

of the samples exhibited a 3DOM architecture, and the cobalt oxide nanoparticles attaching to the surface of the macropore walls were rather uniform with an average diameter of 7–11 nm, especially those on the $10\text{CoO}_x/3\text{DOM-ESFO}$ surfaces (Fig. 3j and k). A close observation on the high-resolution TEM images (Fig. 3d, f, i, and l) reveals that in addition to the exposed (1 1 2) lattice plane of the 3DOM-ESFO support, the mainly exposed lattice planes of the $y\text{CoO}_x/3\text{DOM-ESFO}$ samples were (3 1 1) crystal plane, and the lattice spacings (d value) of the cobalt oxide nanoparticles were estimated to be in the range of 0.24–0.25 nm, rather close to that (0.244 nm) of the standard Co_3O_4 sample (JCPDS PDF# 42-1467). Furthermore, there was the exposure of (2 2 4) lattice plane in the $6\text{CoO}_x/3\text{DOM-ESFO}$ and $10\text{CoO}_x/3\text{DOM-ESFO}$ samples. The recording of multiple bright electron diffraction rings in the SAED patterns (insets of Fig. 3d, f, i, and l) demonstrates that the 3DOM-ESFO and $y\text{CoO}_x/3\text{DOM-ESFO}$ samples were polycrystalline.

N_2 adsorption–desorption isotherms and pore-size distributions of the 3DOM-ESFO and $y\text{CoO}_x/3\text{DOM-ESFO}$ samples are shown in Fig. 4. It is seen from Fig. 4A that all of the samples displayed a similar type II isotherm with H3 ($p/p_0 = 0.9\text{--}1.0$) and H2 ($p/p_0 = 0.2\text{--}0.9$) hysteresis loops, indicating that these samples were materials with macroporous and mesoporous structures [29,35]. Such highly developed porous structures would provide the facile adsorption and diffusion of reactant molecules, thus avoiding limitations of interphase mass transfer and hence enhancing the catalytic activity. There was a difference in the size of H3 or H2 hysteresis loop between 3DOM-ESFO and $y\text{CoO}_x/3\text{DOM-ESFO}$, demonstrating that the 3DOM structure was modified by the loaded cobalt oxides, which also played a role in influencing the pore-size distributions (Fig. 4B) and BET surface areas (Table 1) of $y\text{CoO}_x/3\text{DOM-ESFO}$. It is worth mentioning that there were a number of nanovoids with the diameter of 2–8 nm on the skeletons of the 3DOM-ESFO support. From Fig. 4B, one can see that the 3DOM-ESFO support displayed one broad pore-size distribution centered at ca. 35 nm, whereas the $y\text{CoO}_x/3\text{DOM-ESFO}$ samples showed two noticeable pore-size distributions centered at different pore sizes. The 3DOM-ESFO sample possessed the largest surface area ($31.3\text{ m}^2\text{ g}^{-1}$) due to the thinner wall and the presence of nanovoids. The surface area increased with a rise in cobalt oxide loading from $y\text{wt}\% = 1$ to 6, but it decreased to $22.4\text{ m}^2\text{ g}^{-1}$ when $y\text{wt}\% = 10$. Considering the variation tendency of $dV/d(\log D)$ in the pore size range of 1.7–4.0 nm, there might be a trace amount of micropores in the structure of the samples except for $10\text{CoO}_x/3\text{DOM-ESFO}$. In addition, the pore volumes of $1\text{CoO}_x/3\text{DOM-ESFO}$, $3\text{CoO}_x/3\text{DOM-ESFO}$, and $6\text{CoO}_x/3\text{DOM-ESFO}$ were nearly twice as those of 3DOM-ESFO and $10\text{CoO}_x/3\text{DOM-ESFO}$ (Table 1).

3.3. Surface composition, metal oxidation states, and oxygen species

The Eu 3d and Sr 3d XPS spectra (Fig. S1 of the Supplementary material) of the 3DOM-ESFO and $y\text{CoO}_x/3\text{DOM-ESFO}$ samples indicate that Eu and Sr were tri- and divalent, respectively. Fig. 5 illustrates the Fe $2p_{3/2}$ and O 1s spectra of the 3DOM-ESFO and $y\text{CoO}_x/3\text{DOM-ESFO}$ samples. It is observed from Fig. 5A that there was one asymmetrical signal, which can be decomposed into two components at BE = ca. 710.4 and 712.6 eV, ascribable to the surface Fe^{3+} and Fe^{4+} species [36], respectively. The asymmetrical Co $2p_{3/2}$ signal of $y\text{CoO}_x/3\text{DOM-ESFO}$ can be decomposed into two components at BE = 779.8 eV and 782.1 eV (Fig. 4B), assignable to the surface Co^{3+} and Co^{2+} species [37,38], respectively. The surface element compositions of the samples are summarized in Table 2. The M'/M ($M' = \text{Eu, Sr, Fe, and Co}$) atomic ratios in ESFO and $y\text{CoO}_x/3\text{DOM-ESFO}$ indicate that there was surface Eu enrichment on each of the samples. The $\text{Fe}^{3+}/\text{Fe}^{4+}$ molar ratios

of these samples were basically same (1.01–1.03), whereas the $\text{Co}^{3+}/\text{Co}^{2+}$ molar ratios were smaller than the theoretical value (2.0) of Co_3O_4 , and varied with the loading of cobalt oxide. As demonstrated in Fig. 4C, the asymmetrical O 1s XPS signal of each of the samples could be decomposed into two components at BE = ca. 528.9 and 531.4 eV, attributable to the lattice oxygen species (O_{latt}) and surface adsorbed oxygen species (O_{ads} , e.g. O_2^- , O_2^{2-} or O^-) [39–41], respectively. No significant O 1s signals at BE = ca. 533.2 eV assignable to the surface carbonate species [33,42,43] were detected. As shown in Fig. S1(E) of the Supplementary material, the signal due to the surface carbonate species was rather weak, indicating that there was a trace amount of surface carbonate species on the catalysts. The surface $\text{O}_{\text{ads}}/\text{O}_{\text{latt}}$ molar ratios decreased in the order of $6\text{CoO}_x/3\text{DOM-ESFO}$ (2.59) > $3\text{CoO}_x/3\text{DOM-ESFO}$ (2.48) > $10\text{CoO}_x/3\text{DOM-ESFO}$ (2.37) > $1\text{CoO}_x/3\text{DOM-ESFO}$ (2.22) > 3DOM-ESFO (1.53). It is known that the higher the surface oxygen vacancy density, the easier are the adsorption and activation of O_2 molecules, and thus the better is the catalytic performance of ABO_3 for the combustion of VOCs [37]. Such a deduction was further proved by the following H_2 -TPR measurements and catalytic activity tests for toluene combustion of these samples.

3.4. Reducibility

H_2 -TPR technique was used to evaluate reducibility of the perovskite samples. Fig. 6 illustrates the H_2 -TPR profiles of 3DOM-ESFO and $y\text{CoO}_x/3\text{DOM-ESFO}$ samples. It is observed from Fig. 6A(a) that there were two main reduction steps in the temperature ranges of 50–550 °C and 550–900 °C, respectively. The former was due to the reduction of Fe^{4+} to Fe^{3+} as well as the removal of O_{ads} , whereas the latter was due to the reduction of Fe^{3+} to Fe^{2+} or even metallic Fe^0 [36]. With the loading of cobalt oxide, new reduction bands centered at around 300 and 440 °C of the $y\text{CoO}_x/3\text{DOM-ESFO}$ (Fig. 6A(b–e)) could be attributed to the reduction of Co^{3+} to Co^{2+} and Co^{2+} to Co^0 [26,37,44,45], respectively, but the original bands at ca. 240, 400, 520, 609, and 721 °C (corresponding to the reduction of $\text{Fe}^{4+} \rightarrow \text{Fe}^{3+}$ and $\text{Fe}^{3+} \rightarrow \text{Fe}^{2+}$) and 802 °C (corresponding to the reduction of $\text{Fe}^{2+} \rightarrow \text{Fe}^0$) shifted to lower temperatures by 10–30 °C, and the original reduction band at 217 °C (Fig. 6A(a)) due to the removal of O_{ads} [46] on the ESFO surface was replaced by the bands at 110–190 °C (Fig. 6A(b–e)) due to the removal of O_{ads} on highly dispersed Co_3O_4 or the interface between Co_3O_4 nanoparticles and the 3DOM-ESFO support. Quite similar phenomena have been reported in the cases of LaMnO_3 and $\text{LaMn}_{1-x}\text{O}_{3+\delta}$ ($x = 0.05\text{--}0.4$) [23]. The reduction pattern for $10\text{CoO}_x/3\text{DOM-ESFO}$ was somewhat different from the ones obtained for the samples with lower cobalt oxide loadings due to the excessive aggregation of cobalt oxide phase. The shape and intensity of the reduction bands of the $y\text{CoO}_x/3\text{DOM-ESFO}$ samples varied from each other, a result due to the different accessibilities to the support. It was reported that when the content of high-valence metal cations rose, the chemical potential and reactivity of oxygen adjacent to the metal cations would be promoted, giving rise to the rapid desorption of oxygen at lower temperatures [47]. Jung and Bell [48] reported that the surface of metal could activate hydrogen molecules to catalyze the reduction of other metal ions. That is to say, the generated metallic cobalt would play a role in the reduction of 3DOM-ESFO at higher temperatures. Therefore, a synergistic effect between Co_3O_4 and ESFO is expected to exist. From Table 2, one can see that with the rise in cobalt oxide loading, the H_2 consumption of the sample in the range of 50–550 °C increased but that above 550 °C decreased, a result due to the enhanced reduction of cobalt oxide.

It is known that the reducibility of a catalyst can be effectively evaluated by using the initial (where less than 25% oxygen in the sample was consumed for the first reduction band) H_2

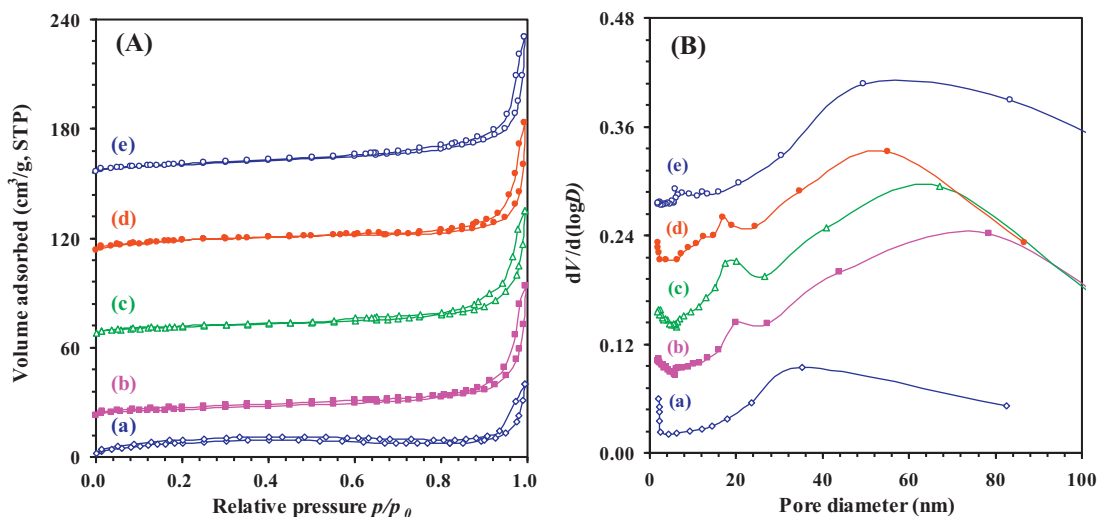


Fig. 4. (A) Nitrogen adsorption–desorption isotherms and (B) pore-size distributions of (a) 3DOM-ESFO, (b) 1CoO_x/3DOM-ESFO, (c) 3CoO_x/3DOM-ESFO, (d) 6CoO_x/3DOM-ESFO, and (e) 10CoO_x/3DOM-ESFO.

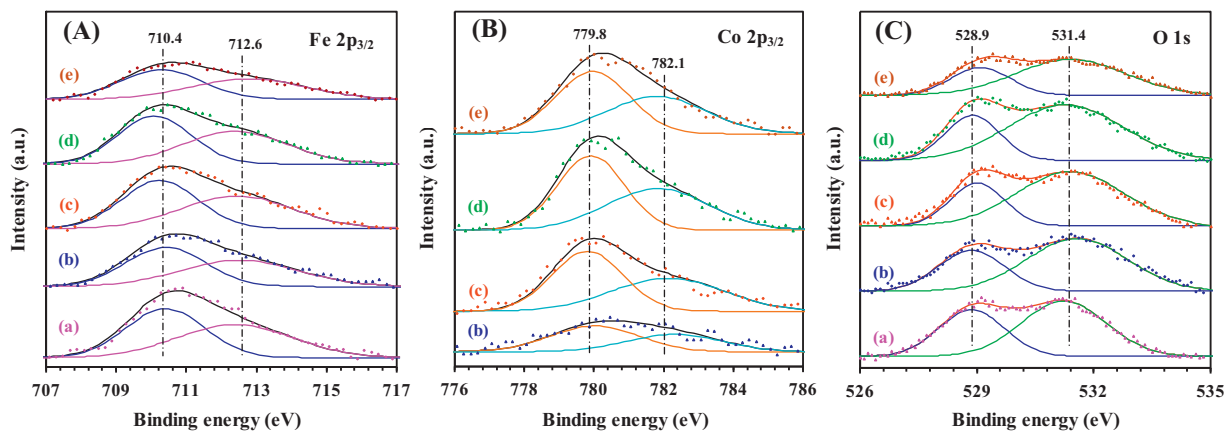


Fig. 5. (A) Fe 2p_{3/2}, (B) Co 2p_{3/2}, and (C) O 1s XPS spectra of (a) 3DOM-ESFO, (b) 1CoO_x/3DOM-ESFO, (c) 3CoO_x/3DOM-ESFO, (d) 6CoO_x/3DOM-ESFO, and (e) 10CoO_x/3DOM-ESFO.

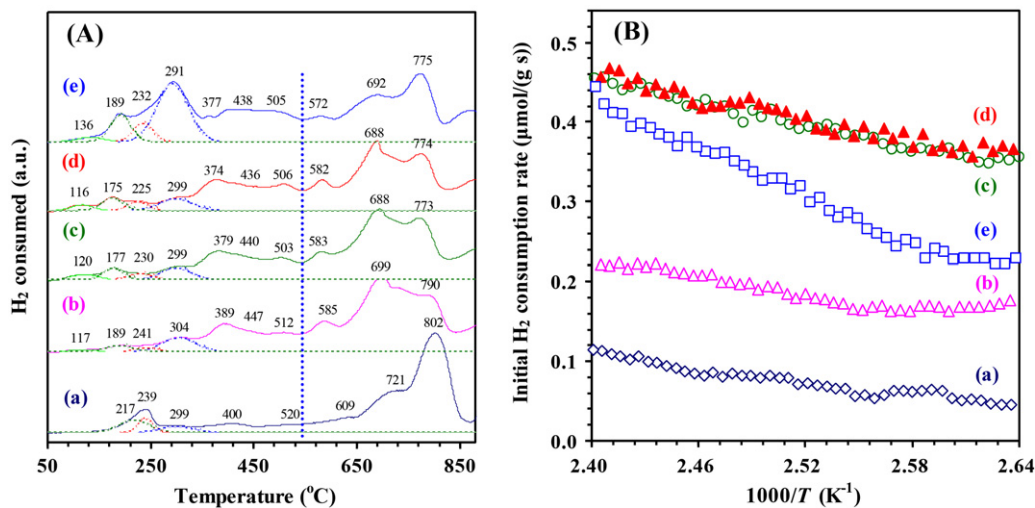


Fig. 6. (A) H₂-TPR profiles and (B) initial H₂ consumption rate as a function of inverse temperature of (a) 3DOM-ESFO, (b) 1CoO_x/3DOM-ESFO, (c) 3CoO_x/3DOM-ESFO, (d) 6CoO_x/3DOM-ESFO, and (e) 10CoO_x/3DOM-ESFO.

Table 2Surface element compositions and H₂ consumptions of the 3DOM-ESFO and yCoO_x/3DOM-ESFO catalysts.

Catalyst	Surface element composition							H ₂ consumption ^a (mmol g ^{−1})	
	Eu/M ^b	Sr/M ^b	Fe/M ^b	Co/M ^b	Fe ³⁺ /Fe ⁴⁺	Co ³⁺ /Co ²⁺	O _{ads} /O _{latt}	50–550 °C	550–880 °C
3DOM-ESFO	0.638 (0.3)	0.063 (0.2)	0.299 (0.5)	–	1.01	–	1.53	1.66	5.48
1CoO _x /3DOM-ESFO	0.549 (0.3)	0.089 (0.2)	0.361 (0.5)	0.14	1.01	1.39	2.22	2.35	5.20
3CoO _x /3DOM-ESFO	0.543 (0.3)	0.074 (0.2)	0.382 (0.5)	0.16	1.01	1.14	2.48	2.72	5.09
6CoO _x /3DOM-ESFO	0.541 (0.3)	0.070 (0.2)	0.389 (0.5)	0.22	1.03	1.17	2.59	2.96	4.71
10CoO _x /3DOM-ESFO	0.542 (0.3)	0.067 (0.2)	0.392 (0.5)	0.25	1.03	1.23	2.37	4.85	4.56

^a The data were obtained by quantitatively analyzing the H₂-TPR profiles.^b M = Eu + Sr + Fe, and the data in parenthesis are the nominal M'/M (M' = Eu, Sr, Fe, and Co) atomic ratios in ESFO.

consumption rate [49,50]. Fig. 6B shows the initial H₂ consumption rate versus inverse temperature (in the range of 105–143 °C) of the 3DOM-ESFO and yCoO_x/3DOM-ESFO samples. It can be clearly seen that the initial H₂ consumption rates (i.e., the reducibility at low temperature) of the samples followed the sequence of 6CoO_x/3DOM-ESFO > 3CoO_x/3DOM-ESFO > 10CoO_x/3DOM-ESFO > 1CoO_x/3DOM-ESFO > 3DOM-ESFO. The trends are in good agreement with the orders of surface adsorbed oxygen concentration and catalytic performance shown below.

3.5. Catalytic performance

When only quartz sands were loaded into the microreactor (Fig. S2(A) of the Supplementary material), we did not detect significant conversion of toluene below 400 °C, and the light-off temperature of the homogeneous reaction was 450 °C. This result indicates that no homogeneous reactions took place under the conditions of toluene concentration = 1000 ppm, toluene/O₂ molar ratio = 1/400, and SV = 20,000 mL g^{−1} h^{−1}. Fig. 7A shows the catalytic performance of the 3DOM-ESFO and yCoO_x/3DOM-ESFO samples for the combustion of toluene. It is noted that CO₂ and H₂O were the only products of toluene combustion over these catalyst samples and carbon balance was ca. 99.5% in each catalytic run. From Fig. 7A, one can observe that the catalytic activity increased with reaction temperature, and followed a sequence of 6CoO_x/3DOM-ESFO > 3CoO_x/3DOM-ESFO > 10CoO_x/3DOM-ESFO > 1CoO_x/3DOM-ESFO > 3DOM-ESFO. The reaction temperatures *T*_{10%}, *T*_{50%}, and *T*_{90%} (corresponding to toluene conversion = 10, 50, and 90%) are usually used to evaluate the activity of a catalyst, as summarized in Table 3. Obviously, the 6CoO_x/3DOM-ESFO > 3CoO_x/3DOM-ESFO catalysts performed the best, giving the *T*_{10%}, *T*_{50%}, and *T*_{90%} of 220–225, 251, 268–270 °C, respectively, which was much better than that (*T*_{10%} = 233 °C, *T*_{50%} = 278 °C, and *T*_{90%} = 305 °C) of the 3DOM-ESFO catalyst. Fig. 7B shows the effect of SV on the catalytic activity of the 3CoO_x/3DOM-ESFO sample. As expected, toluene conversion increased as the SV dropped. The *T*_{10%}, *T*_{50%}, and *T*_{90%} values obtained over 3CoO_x/3DOM-ESFO were 207, 244, and 255 °C at SV = 10,000 mL g^{−1} h^{−1}, whereas they were 226, 255, and 278 °C at SV = 40,000 mL g^{−1} h^{−1}, respectively. The on-stream catalytic test result (Fig. S2(B) of the Supplementary material) indicates that the 3CoO_x/3DOM-ESFO sample was catalytically stable within 100 h of on-stream reaction. The used sample exhibited a surface area of 23.3 m² g^{−1}, not far away from that (24.1 m² g^{−1}) of the fresh sample.

For the purpose of better comparison on the catalytic performance of catalysts, the specific toluene consumption rate (*r*) normalized per catalyst mass was calculated, and the results are shown in Fig. 7C. Obviously, all of the curves kept the shapes same as the ones of toluene conversion versus reaction temperature (Fig. 7A), and among the 3DOM-ESFO and yCoO_x/3DOM-ESFO catalysts the 6CoO_x/3DOM-ESFO and 3CoO_x/3DOM-ESFO ones

exhibited the highest catalytic performance for toluene combustion.

It has been demonstrated that the oxidation of VOCs over perovskite-type oxides in the presence of excess oxygen would obey the first-order reaction mechanism toward the VOC concentration (i.e., $r = kc = [A \exp(-E_a/RT)]c$) [51], in which the rate constant *k* (s^{−1}), apparent activation energy *E*_a (kJ mol^{−1}), and pre-exponential factor *A* (s^{−1}) for each of the samples could be calculated from the corresponding toluene conversion (*X*% < 20%), specific toluene consumption rate *r* (μmol g^{−1} s^{−1}) at the reaction temperature, and the slope of its Arrhenius plot (Fig. 7D), respectively, and the results are summarized in Table 3. The rather close to 1 of the correlation coefficients (*R*²) of the Arrhenius plots for all of the catalyst samples indicates the excellent linear relationship of ln*k* versus 1000/*T*. From the *E*_a values estimated from the slopes of the Arrhenius plots, one can observe that the activation energy followed a sequence of 6CoO_x/3DOM-ESFO (71.6 kJ mol^{−1}) < 3CoO_x/3DOM-ESFO (72.3 kJ mol^{−1}) < 10CoO_x/3DOM-ESFO (73.5 kJ mol^{−1}) < 1CoO_x/3DOM-ESFO (77.7 kJ mol^{−1}) < 3DOM-ESFO (81.1 kJ mol^{−1}), in good agreement with the inverse orders of oxygen adspecies concentration and low-temperature reducibility.

Under similar reaction conditions (SV = 20,000 mL g^{−1} h^{−1}), the catalytic performance (*T*_{50%} = 251 °C and *T*_{90%} = 268–270 °C) of 6CoO_x/3DOM-ESFO and 3CoO_x/3DOM-ESFO was much better than that of 3DOM SrFeO_{3–δ} (*T*_{50%} = 292 °C and *T*_{90%} = 340 °C) [33], mesoporous yLaCoO₃/SBA-15 (*y* = 10–50 wt%; *T*_{50%} > 300 °C and *T*_{90%} > 320 °C) [52], bulk LaCoO₃ (*T*_{50%} = 252 °C and *T*_{90%} = 290 °C) [52], La_{0.6}Sr_{0.4}CoO₃ (*T*_{50%} = 310 °C and *T*_{90%} = 320 °C) [53], and bulk Co₃O₄ (*T*_{50%} = 265 °C and *T*_{90%} = 288 °C) [44], but they were inferior to that of 3DOM LaMnO₃ (*T*_{50%} = 222 °C and *T*_{90%} = 243 °C at SV = 20,000 mL g^{−1} h^{−1}) [31], La_{0.6}Sr_{0.4}FeO₃ (*T*_{50%} = 235 °C and *T*_{90%} = 256 °C) [53], mesoporous Co₃O₄ (*T*_{50%} = 164 °C and *T*_{90%} = 198 °C) [44], and Co₃O₄/KIT6 or Co₃O₄/SBA16 (*T*_{50%} = 143 °C and *T*_{90%} = 175 °C) [37].

It is widely accepted that the catalytic activity of either a ABO₃ material or a simple transition metal oxide MO_x is always related to the factors, such as the unusual oxidation states of the transition metal ions, defect nature and density, nonstoichiometric oxygen concentration, and reducibility [54,55]. It is well accepted that the oxidation of organic molecules over the transition metal oxide and mixed metal oxide catalysts involves a Mars–van Krevelen mechanism, where the organic molecule is oxidized by the lattice oxygen of metal oxides and mixed metal oxides, the latter being re-oxidized by gas-phase oxygen [56–61]. In the case of ESFO and yCoO_x/3DOM-ESFO, the lattice oxygen of the catalysts can be consumed by reaction with toluene and then be replenished by oxygen from the gas phase [62–64]. Thus, the lattice oxygen of ESFO and yCoO_x/3DOM-ESFO can be of great importance in the catalytic oxidation of toluene. The reducibility at low temperature reflects the reactivity of the lattice oxygen in ESFO and yCoO_x/3DOM-ESFO. As shown in Fig. 6A and B, the lattice oxygen reactivity decreased in the order

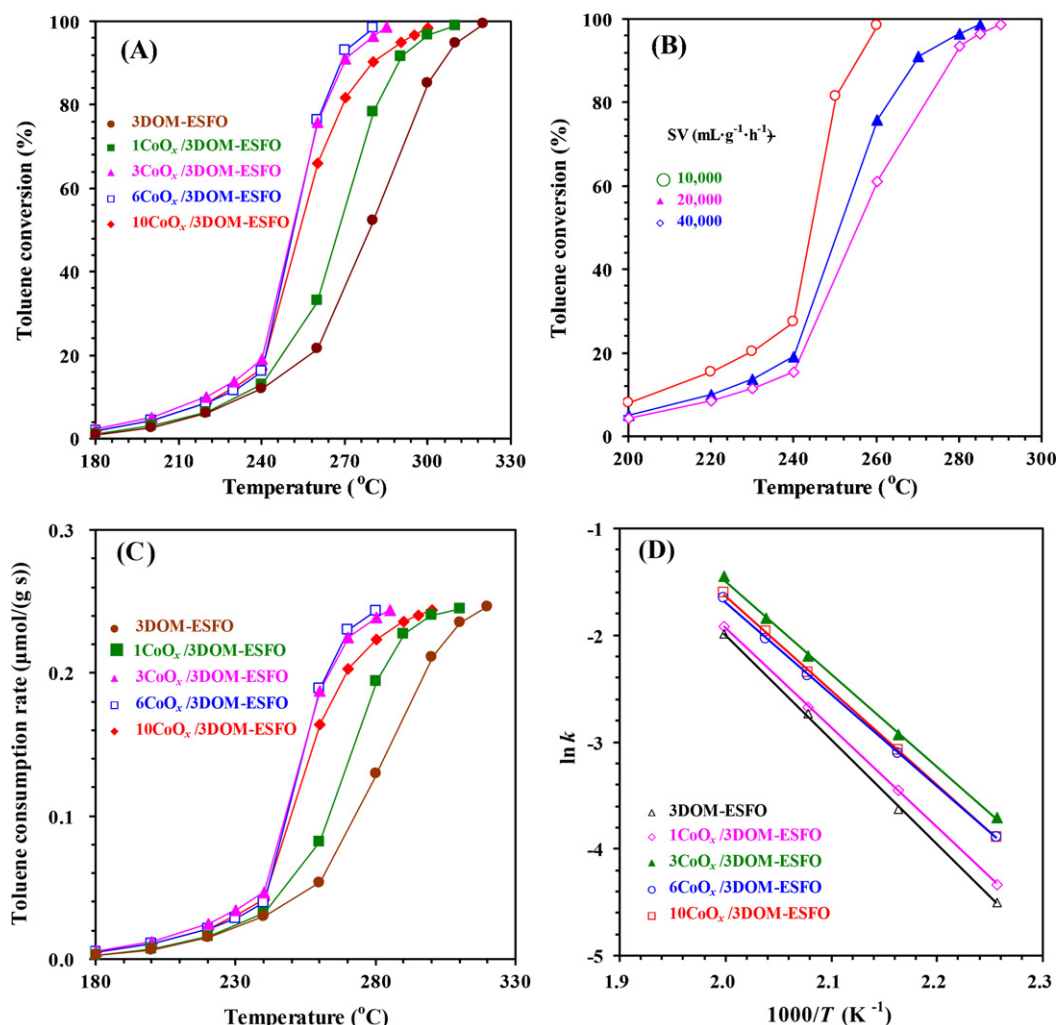


Fig. 7. (A) Toluene conversion as a function of reaction temperature over the 3DOM-ESFO and $\gamma\text{CoO}_x/3\text{DOM-ESFO}$ catalysts under the conditions of toluene concentration = 1000 ppm, toluene/oxygen molar ratio = 1/400, and $\text{SV} = 20,000 \text{ mL g}^{-1} \text{ h}^{-1}$, (B) toluene conversion over the $3\text{CoO}_x/3\text{DOM-ESFO}$ catalyst at different SV values, (C) toluene consumption rate versus reaction temperature over the 3DOM-ESFO and $\gamma\text{CoO}_x/3\text{DOM-ESFO}$ catalysts, and (D) Arrhenius plots for the 3DOM-ESFO and $\gamma\text{CoO}_x/3\text{DOM-ESFO}$ catalysts.

of $6\text{CoO}_x/3\text{DOM-ESFO} \approx 3\text{CoO}_x/3\text{DOM-ESFO} > 10\text{CoO}_x/3\text{DOM-ESFO} > 1\text{CoO}_x/3\text{DOM-ESFO} > 3\text{DOM-ESFO}$, in basic agreement with the sequence of the catalytic performance of these samples ($6\text{CoO}_x/3\text{DOM-ESFO} > 3\text{CoO}_x/3\text{DOM-ESFO} > 10\text{CoO}_x/3\text{DOM-ESFO} > 1\text{CoO}_x/3\text{DOM-ESFO} > 3\text{DOM-ESFO}$). The formation of surface oxygen vacancies has also an important role to play. These defective sites can be the active centers in the catalytic reaction since oxygen of defective oxides tends to be readily released and transferred, which would enhance the reactivity of the catalysts in oxidation of VOCs [65,66]. As we know, the nonstoichiometric oxygen is also associated with structural defects and can be converted from

O_2^- (the lowest reactivity) to O^- (the highest reactivity) at elevated temperatures [55]. Regularly, a higher structural defect density and a stronger reducibility endow the catalyst with better catalytic performance [67]. Besides, a high surface area is usually beneficial for the improvement of catalytic activity [31,44,68]. In the present work, however, it seems that surface area of the sample was a minor factor influencing the catalytic performance, but oxygen adspecies concentration (revealed by the XPS studies) and the reducibility at low temperature (demonstrated by the H_2 -TPR investigations) are the important factors influencing the catalytic activity. Therefore, we conclude that the good catalytic

Table 3
Catalytic activities of the 3DOM-ESFO and $\gamma\text{CoO}_x/3\text{DOM-ESFO}$ catalysts under the conditions of toluene concentration = 1000 ppm, toluene/oxygen molar ratio = 1/400, and $\text{SV} = 20,000 \text{ mL g}^{-1} \text{ h}^{-1}$ rate constants (k), specific reaction rates (r), activation energies (E_a), pre-exponential factors (A), and correlation coefficients (R^2) of the plot $\ln k$ versus inverse temperature in the temperature range of 180–240 °C.

Catalyst	Toluene oxidation activity (°C)			$k (\times 10^{-2} \text{ s}^{-1})/r (\times 10^{-3} \mu\text{mol}/(\text{g s}))$					E_a (kJ/mol)	$A (\times 10^6 \text{ s}^{-1})$	R^2
	$T_{10\%}$	$T_{50\%}$	$T_{90\%}$	180 °C	200 °C	220 °C	230 °C	240 °C			
3DOM-ESFO	233	278	305	1.11/2.73	2.67/6.46	6.50/15.2	–/–	13.8/30.1	81.1	35.7	0.9995
$1\text{CoO}_x/3\text{DOM-ESFO}$	231	267	289	1.32/3.22	3.20/7.69	6.95/16.1	–/–	14.8/32.0	77.7	12.0	0.9999
$3\text{CoO}_x/3\text{DOM-ESFO}$	220	251	270	2.46/5.94	5.37/12.6	11.2/25.0	16.0/34.2	23.6/47.3	72.3	5.27	0.9993
$6\text{CoO}_x/3\text{DOM-ESFO}$	225	251	268	2.04/4.95	4.49/10.6	9.29/21.0	13.1/28.7	19.2/39.9	71.6	3.65	0.9995
$10\text{CoO}_x/3\text{DOM-ESFO}$	224	253	279	2.04/4.96	4.60/10.9	9.53/21.6	14.0/30.5	20.2/41.7	73.5	5.95	0.9995

performance of $3\text{CoO}_x/3\text{DOM-ESFO}$ and $6\text{CoO}_x/3\text{DOM-ESFO}$ for toluene combustion was mainly related to the higher oxygen adspecies concentration and better reducibility at low temperature. In addition, the 3DOM structure of ESFO with nanovoid skeletons would reduce the diffusion limitations of reactant molecules and guaranteed the good dispersion of cobalt oxide nanoparticles. Thus, 3DOM structure of ESFO was considered to be another reason for the enhanced catalytic performance for toluene combustion.

4. Conclusions

3DOM-structured $\text{Eu}_{0.6}\text{Sr}_{0.4}\text{FeO}_3$ (3DOM-ESFO) and $\gamma\text{CoO}_x/3\text{DOM-ESFO}$ ($\gamma\text{wt}\% = 1, 3, 6, \text{ and } 10$) were prepared by using citrate acid-assisted PMMA-templating and incipient wetness impregnation methods, respectively. All of the supported samples retained a high-quality 3DOM architecture with a surface area of $22\text{--}31\text{ m}^2\text{ g}^{-1}$. The cobalt oxide nanoparticles with a diameter of $7\text{--}9\text{ nm}$ were highly dispersed on the surface of the 3DOM support. The surface oxygen species concentration and low-temperature reducibility followed a sequence of $3\text{CoO}_x/3\text{DOM-ESFO} \approx 6\text{CoO}_x/3\text{DOM-ESFO} > 10\text{CoO}_x/3\text{DOM-ESFO} > 1\text{CoO}_x/3\text{DOM-ESFO} > 3\text{DOM-ESFO}$, coinciding with the order of their catalytic performance. The $3\text{CoO}_x/3\text{DOM-ESFO}$ and $6\text{CoO}_x/3\text{DOM-ESFO}$ performed the best, giving the $T_{50\%}$ and $T_{90\%}$ of ca. 250 and 270°C at $\text{SV} = 20,000\text{ mL g}^{-1}\text{ h}^{-1}$, respectively. The apparent activation energies (ca. 72 kJ mol^{-1}) of $3\text{CoO}_x/3\text{DOM-ESFO}$ and $6\text{CoO}_x/3\text{DOM-ESFO}$ samples were much lower than that (81 kJ mol^{-1}) of the 3DOM-ESFO support. Based on the characterization results and catalytic activity data, we conclude that the high oxygen adspecies concentration, good reducibility at low temperature, and high dispersion of cobalt oxide nanoparticles were responsible for the good catalytic performance of $3\text{CoO}_x/3\text{DOM-ESFO}$ and $6\text{CoO}_x/3\text{DOM-ESFO}$ for toluene combustion.

Acknowledgments

The work was supported by the NSF of China (20973017 and 21077007), the NSF of Beijing Municipality (2102008), the Discipline and Postgraduate Education (005000541212014), the Creative Research Foundation of Beijing University of Technology (00500054R4003 and 005000543111501), the National High-Tech Research and Development (863) Key Program of Ministry of Science and Technology of China (2009AA063201), and the Funding Project for Academic Human Resources Development in Institutions of Higher Learning under the Jurisdiction of Beijing Municipality (PHR201007105 and PHR201107104). We also thank Prof. Chak Tong Au (Department of Chemistry, Hong Kong Baptist University) and Mrs. Jianping He (State Key Laboratory of Advanced Metals & Materials, University of Science and Technology Beijing) for doing the XPS and SEM analyses, respectively.

Appendix A. Supplementary data

Supplementary data associated with this article can be found, in the online version, at <http://dx.doi.org/10.1016/j.apcatb.2012.10.005>.

References

- [1] M. Alifanti, M. Florea, G. Filotti, V. Kuncser, V. Cortes-Corberan, V.I. Parvulescu, *Catalysis Today* 117 (2006) 329–336.
- [2] V. Blasin-Aubé, J. Belkouch, L. Monceaux, *Applied Catalysis B: Environmental* 43 (2003) 175–186.
- [3] S.A. Hosseini, M.T. Sadeghi-Sorkhani, L. Kafi-Ahmadi, A. Alemi, A. Niaei, D. Salari, *Chinese Journal of Catalysis* 32 (2011) 1465–1468.
- [4] W.B. Li, J.X. Wang, H. Gong, *Catalysis Today* 148 (2009) 81–87.
- [5] J.-M. Giraudon, A. Elhachimi, F. Wyrwalski, S. Siffert, A. Aboukais, J.-F. Lamonier, G. Leclercq, *Applied Catalysis B: Environmental* 75 (2007) 157–166.
- [6] S. Rousseau, S. Lorient, P. Delichere, A. Boreave, J.P. Deloume, P. Vernoux, *Applied Catalysis B: Environmental* 88 (2009) 438–447.
- [7] R. Pereñíguez, J.L. Hueso, F. Gaillard, J.P. Holgado, A. Caballero, *Catalysis Letters* 142 (2012) 408–416.
- [8] L.F. Liotta, M. Ousmane, G.D. Carlo, G. Pantaleo, G. Deganello, A. Boreave, A. Giroir-Fendler, *Catalysis Letters* 127 (2009) 270–276.
- [9] M.A. Peña, J.L.G. Fierro, *Chemical Reviews* 101 (2001) 1981–2018.
- [10] S. Petrovic, A. Terlecki-Barievic, L. Karanovic, P. Kirilov-Stefanov, M. Zdujic, V. Dondur, D. Paneva, I. Mitov, V. Rakic, *Applied Catalysis B: Environmental* 79 (2008) 186–198.
- [11] S. Irueta, M.P. Pina, M. Menedez, J. Santamaria, *Journal of Catalysis* 179 (1998) 400–412.
- [12] H.-J. Eom, J.H. Jang, D.-W. Lee, S. Kim, K.-Y. Lee, *Journal of Molecular Catalysis A: Chemical* 349 (2011) 48–54.
- [13] A. Hartley, M. Sahibzada, M. Weston, I.S. Metcalfe, D. Mantzavinos, *Catalysis Today* 55 (2000) 197–204.
- [14] M. Sadakane, T. Horiuchi, N. Kato, K. Sasaki, W. Ueda, *Journal of Solid State Chemistry* 183 (2010) 1365–1371.
- [15] M. Sadakane, T. Asanuma, J. Kubo, W. Ueda, *Chemistry of Materials* 17 (2005) 3546–3551.
- [16] Y.C. Wei, J. Liu, Z. Zhao, Y.S. Chen, C.M. Xu, A.J. Duan, G.Y. Jiang, H. He, *Angewandte Chemie International Edition* 50 (2011) 2326–2329.
- [17] J.F. Xu, J. Liu, Z. Zhao, J.X. Zheng, G.Z. Zhang, A.J. Duan, G.Y. Jiang, *Catalysis Today* 153 (2010) 136–142.
- [18] J.F. Xu, J. Liu, Z. Zhao, C.M. Xu, J.X. Zheng, A.J. Duan, G.Y. Jiang, *Journal of Catalysis* 282 (2011) 1–12.
- [19] D. Delimaris, T. Ioannides, *Applied Catalysis B: Environmental* 84 (2008) 303–312.
- [20] B. Solsona, I. Vázquez, T. García, T.E. Davies, S.H. Taylor, *Catalysis Letters* 116 (2007) 116–121.
- [21] J.C. Zhou, D.F. Wu, W. Jiang, Y.D. Li, *Chemical Engineering & Technology* 32 (2009) 1520–1526.
- [22] K.M. Ji, H.X. Dai, J.X. Dai, J.G. Deng, F. Wang, H. Zhang, L. Zhang, *Catalysis Today*, <http://dx.doi.org/10.1016/j.cattod.2012.03.061>, in press.
- [23] P. Esmailnejad-Ahranjani, A. Khodadadi, H. Ziaei-Azad, Y. Mortazavi, *Chemical Engineering Journal* 169 (2011) 282–289.
- [24] M. Alifanti, M. Florea, S. Somacescu, V.I. Parvulescu, *Applied Catalysis B: Environmental* 60 (2005) 33–39.
- [25] L. Simonot, F. Garin, G. Maire, *Applied Catalysis B: Environmental* 11 (1997) 167–179.
- [26] Y.Z. Fang, Y. Liu, L.H. Zhang, *Applied Catalysis A: General* 397 (2011) 183–191.
- [27] A. Galenda, M.M. Natile, V. Krishnan, H. Bertagnolli, A. Glisenti, *Chemistry of Materials* 19 (2007) 2796–2808.
- [28] A. Galenda, M.M. Natile, A. Glisenti, *Journal of Molecular Catalysis A: Chemical* 282 (2008) 52–61.
- [29] H.N. Li, L. Zhang, H.X. Dai, H. He, *Inorganic Chemistry* 48 (2009) 4421–4434.
- [30] R.Z. Zhang, H.X. Dai, Y.C. Du, L. Zhang, J.G. Deng, Y.S. Xia, Z.X. Zhao, X. Meng, Y.X. Liu, *Inorganic Chemistry* 50 (2011) 2534–2544.
- [31] Y.X. Liu, H.X. Dai, Y.C. Du, J.G. Deng, L. Zhang, Z.X. Zhao, C.T. Au, *Journal of Catalysis* 287 (2012) 149–160.
- [32] Y.X. Liu, H.X. Dai, Y.C. Du, J.G. Deng, L. Zhang, Z.X. Zhao, *Applied Catalysis B: Environmental* 119–120 (2012) 20–31.
- [33] K.M. Ji, H.X. Dai, J.G. Deng, L. Zhang, F. Wang, H.Y. Jiang, C.T. Au, *Applied Catalysis A: General* 425–426 (2012) 153–160.
- [34] L.F. Liotta, M. Ousmane, G. Di Carlo, G. Pantaleo, G. Deganello, G. Marcic, L. Retailliau, A. Giroir-Fendler, *Applied Catalysis A: General* 347 (2008) 81–88.
- [35] H. Yan, C.F. Blanford, B.T. Holland, W.H. Smyrl, A. Stein, *Chemistry of Materials* 12 (2000) 1134–1141.
- [36] H. Falcon, J.A. Barbero, J.A. Alonso, M.J. Martinez-Lope, J.L.G. Fierro, *Chemistry of Materials* 14 (2002) 2325–2333.
- [37] Y.S. Xia, H.X. Dai, H.Y. Jiang, L. Zhang, *Catalysis Communications* 11 (2010) 1171–1175.
- [38] C.V. Schenck, J.G. Dillard, J.W. Murray, *Journal of Colloid and Interface Science* 95 (1983) 398–409.
- [39] L.G. Tejuca, J.L.G. Fierro, J.M.D. Tascon, *Advances in Catalysis* 36 (1989) 237–328.
- [40] A. Majid, J. Tunney, S. Argue, D. Wang, M. Post, J. Margeson, *Journal of Alloys and Compounds* 398 (2005) 48–54.
- [41] M.W. Roberts, *Chemical Society Reviews* 18 (1989) 451–475.
- [42] A. Machocki, T. Ioannides, B. Stasinska, W. Gac, G. Avgouropoulos, D. Delimaris, W. Grzegorzcyk, S. Pasieczna, *Journal of Catalysis* 227 (2004) 282–296.
- [43] J.R. Niu, J.G. Deng, W. Liu, L. Zhang, G.Z. Wang, H.X. Dai, H. He, X.H. Zi, *Catalysis Today* 126 (2007) 420–429.
- [44] J.G. Deng, L. Zhang, H.X. Dai, Y.S. Xia, H.Y. Jiang, H. Zhang, H. He, *Journal of Physical Chemistry C* 114 (2010) 2694–2700.
- [45] E. Siebert, C. Roux, A. Boréave, F. Gaillard, P. Vernoux, *Solid State Ionics* 183 (2011) 40–47.
- [46] T.-R. Ling, Z.-B. Chen, M.-D. Lee, *Applied Catalysis A: General* 136 (1996) 191–203.
- [47] H.M. Zhang, Y. Shimizu, Y. Teraoka, N. Miura, N. Yamazoe, *Journal of Catalysis* 121 (1990) 432–440.
- [48] K.D. Jung, A.T. Bell, *Journal of Catalysis* 193 (2000) 207–223.
- [49] K. Chen, S. Xie, A.T. Bell, E. Iglesia, *Journal of Catalysis* 198 (2001) 232–242.
- [50] H.X. Dai, A.T. Bell, E. Iglesia, *Journal of Catalysis* 221 (2004) 491–499.

- [51] S. Cimino, S. Colonna, S. De Rossi, M. Faticanti, L. Lisi, I. Pettiti, P. Portaz, *Journal of Catalysis* 205 (2002) 309–317.
- [52] J.G. Deng, L. Zhang, H.X. Dai, C.T. Au, *Applied Catalysis A: General* 352 (2009) 43–49.
- [53] J.G. Deng, H.X. Dai, H.Y. Jiang, L. Zhang, G.Z. Wang, H. He, C.T. Au, *Environmental Science & Technology* 44 (2010) 2618–2623.
- [54] N.A. Merino, B.P. Barbero, P. Grange, L.E. Cadús, *Journal of Catalysis* 231 (2005) 232–244.
- [55] F. Wang, H.X. Dai, J.G. Deng, G.M. Bai, K.M. Ji, Y.X. Liu, *Environmental Science & Technology* 46 (2012) 4034–4041.
- [56] Y.F. Chang, J.G. McCarty, *Catalysis Today* 30 (1996) 163–170.
- [57] B. Grbic, N. Radic, B. Markovic, P. Stefanov, D. Stoychev, Ts. Marinova, *Applied Catalysis B: Environmental* 64 (2006) 51–56.
- [58] V.P. Santos, M.F.R. Pereira, J.J.M. Órfão, J.L. Figueiredo, *Applied Catalysis B: Environmental* 99 (2010) 353–363.
- [59] R.H. Wang, J.H. Li, *Environmental Science & Technology* 44 (2010) 4282–4287.
- [60] V. Roche, L. Mazri, A. Boréave, M.H. Ta, L. Retailleau-Mevel, A. Giroir-Fendler, P. Vernoux, J.P. Deloume, *Applied Catalysis A: General* 385 (2010) 163–169.
- [61] Y.S. Wu, Y.X. Zhang, M. Liu, Z.C. Ma, *Catalysis Today* 153 (2010) 170–175.
- [62] M. Baldi, E. Finocchio, F. Milella, G. Busca, *Applied Catalysis B: Environmental* 16 (1998) 43–51.
- [63] C. Cellier, V. Ruau, C. Lahousse, P. Grange, E.M. Gaigneaux, *Catalysis Today* 117 (2006) 350–355.
- [64] J. Luo, Q. Zhang, J. Garcia-Martinez, S.L. Suib, *Journal of the American Chemical Society* 130 (2008) 3198–3207.
- [65] X. Chen, Y.F. Shen, S.L. Suib, C.L. O'Young, *Journal of Catalysis* 197 (2001) 292–302.
- [66] Q.H. Tang, T. Liu, Y.H. Yang, *Catalysis Communications* 9 (2008) 2570–2573.
- [67] F.N. Aguero, A. Scian, B.P. Barbero, L.E. Cadus, *Catalysis Letters* 128 (2008) 1–13.
- [68] N. Gunasekaran, S. Saddawi, J.J. Carberry, *Journal of Catalysis* 159 (1996) 107–111.